Mon. Not. R. Astron. Soc. **264,** 961–974 (1993)

# The effects of seeing on the photometric properties of elliptical galaxies

R. P. Saglia,[1,2] Edmund Bertschinger,[3] G. Baggley,[4] David Burstein,[5] Matthew Colless,[6] Roger L. Davies,[4] Robert K. McMahan, Jr[7] and Gary Wegner[4,8]

[1] *Landessternwarte Heidelberg-Königstuhl, Königstuhl, D-69117 Heidelberg 1, Germany*
[2] *Dipartimento di Matematica, via Buonarroti 2, I-56127 Pisa, Italy*
[3] *Department of Physics, MIT, Cambridge, MA 02139, USA*
[4] *Department of Physics, Astrophysics Group, Keble Road, Oxford OX1 3RH*
[5] *Department of Physics and Astronomy, Arizona State University, Tempe, AZ 85287-1504, USA*
[6] *Mount Stromlo and Siding Spring Observatories, Australian National University, Weston Creek, Act 2611, Australia*
[7] *Department of Physics and Astronomy, University of North Carolina, CB# 3255 Phillips Hall, Chapel Hill, NC 27599-3255, USA*
[8] *Department of Physics and Astronomy, Dartmouth College, Wilder Lab., Hanover, NH 03755, USA*

Accepted 1993 May 5. Received 1993 April 15; in original form 1992 December 14

**ABSTRACT**

The effects of seeing on the photometric properties of elliptical galaxies and, in particular, on the $D_n$–$\sigma$ and fundamental plane distance estimators are studied. A new family of functions for the analytical approximation of the point spread function (psf) is introduced and is shown to fit stellar images better than the widely used Gaussian and Moffat functions. Seeing effects are computed for circular mean surface brightness distributions using the $R^{1/4}$ law and models with more and less prominent central cusps. A prescription to correct raw half-luminosity radii, $D_n$ diameters, and surface brightnesses at and within $R_e$ is given. It is shown that seeing effects become important for distant ellipticals ($cz \geq 8000$ km s$^{-1}$). Uncorrected $D_n$–$\sigma$ or fundamental plane distances are systematically too high, leading to spurious negative peculiar velocities of the order of 1000 km s$^{-1}$ at a distance of 12 000 km s$^{-1}$. The large negative peculiar velocities of the most distant clusters of the Faber et al. sample are reduced when seeing effects are taken into account, as is the scatter in the $D_n$–$\sigma$ relation. Seeing corrections are small for galaxies included in the flow solutions of Lynden-Bell et al. (1988) and are unlikely to affect them.

**Key words:** atmospheric effects – methods: data analysis – galaxies: distances and redshifts – galaxies: elliptical and lenticular, cD – galaxies: fundamental parameters – galaxies: photometry.

## 1 INTRODUCTION

The importance of seeing in extragalactic astronomy is well known. Many papers have been written on the subject and much effort has been invested in the construction of new telescopes to minimize its effects. Some subjects of research for which superior seeing conditions during observations, and careful examination of seeing effects during reduction of the data, are required are accurate stellar photometry in crowded fields of galactic globular clusters (Buonanno et al. 1983), studies of cores of extragalactic globular clusters (Bendinelli et al. 1990), detections of 'black holes' or compact dynamical entities in the cores of galaxies (Young et al. 1978; Schweizer 1979; Lauer 1985; Kormendy & Richstone 1992 and references therein), studies of the isophotal shapes of elliptical galaxies (Franx, Illingworth & Heckman 1989; Peletier et al. 1990), classical cosmological tests (Djorgovski 1983), and studies of gravitational lensing effects (Yee 1988). Recent technological developments, combined with the identification of the best sites and the reduction of 'dome-seeing' (see Coulman 1985), have allowed the construction of a new class of ground-based telescopes (e.g. the New Technology Telescope and the Nordic Optical Telescope) with subarcsec seeing image quality.

In contrast, cosmological studies of the large-scale structure and peculiar motions of the Universe have not devoted much attention to the seeing question (see, for example, the conference proceedings edited by Latham & Da Costa 1991, in which the word 'seeing' appears only once). Indeed, redshift surveys (e.g. De Lapparent, Geller & Huchra 1986) gain in efficiency with good seeing conditions but do not require them. Studies of the large-scale motions of galaxies

have been restricted up to now to relatively nearby, large objects. Most of the galaxies of the Seven Samurai sample (Faber et al. 1989) have such large effective radii ($R_e > 20$ arcsec) that no seeing corrections at all are required to obtain reliable $D_n$–$\sigma$ (or fundamental plane) distances (see Section 5).

Seeing effects are more important when these techniques are used to measure the structural properties of typical giant ellipticals at higher redshifts. Seeing scatters light from the inner, centrally concentrated core to the outer, more diffuse regions of ellipticals, producing mean surface brightnesses lower than the true values and larger effective radii. The $D_n$ parameter of the Seven Samurai, defined as the diameter of the aperture enclosing a mean surface brightness of 20.75 $B$ arcsec$^{-2}$, will in turn have a lower measured size. All of this will affect both the distance estimates for these galaxies and their placement with respect to the fundamental plane of ellipticals defined by nearer galaxies (Djorgovski & Davis 1987; Dressler et al. 1987). In particular, seeing will cause the distances of far-away galaxies to be overestimated, producing a spurious negative 'peculiar velocity'.

The EFAR collaboration (the authors of this paper) is currently measuring the distances of a sample of $\approx 550$ elliptical galaxies distributed in 84 clusters of the Hercules–Corona Borealis and Pisces–Cetus superclusters using both the fundamental plane parameters and the $D_n$–$\sigma$ relation as distance estimators. One goal of the project is to detect peculiar motions of amplitude similar to those observed in the Local Supercluster ($\sim 400$–$600$ km s$^{-1}$). Most of the galaxies of the sample have redshifts in the range 8000–15 000 km s$^{-1}$, with typical $R_e$ of 5–10 arcsec, for which we a priori expect seeing effects to be important.

The present paper presents the methodology we have adopted for dealing with this issue. Lucey et al. (1991a) tackled this question using a simplified approach, where $R^{1/4}$-law galaxies are convolved with the Hankel transform of the combined modulation transfer function of the telescope and atmosphere (see Bower, Lucey & Ellis 1992). A fixed value of $R_e$, typical for the galaxies in the cluster under study, is used to compute corrections to the observed aperture magnitudes. The values of $R_e$ and $D_n$ are then derived from these corrected aperture magnitudes. We extend this work by (i) investigating in detail the actual shapes of stellar profiles we observe, (ii) considering different models of elliptical galaxies, and (iii) giving a 'ready to use' prescription to correct the raw values of $R_e$, $D_n$ and the surface brightness at $R_e$ ($SB_e$, in units of mag arcsec$^{-2}$) and within $R_e$ ($\langle SB_e \rangle$, also in mag arcsec$^{-2}$) for seeing.

Section 2 gives the basic equations and discusses the choice of an analytical approximation of the point spread function (psf). In Section 3 a description of the three models of elliptical galaxies used to perform the seeing convolutions is given. The main results of the paper are presented in Section 4 in terms of prescriptions that relate raw $R_e^c$, $D_n^c$, $SB_e^c$ and $\langle SB_e^c \rangle$ values to seeing-free values. Here and throughout the paper the superscript c denotes seeing-convolved quantities. The reader interested in these results, but not concerned about the theoretical details, can refer to Subsection 4.6. A detailed comparison of our method with that of Lucey et al. (1991a) is also given. Section 5 applies the results of Section 4 to galaxies in two representative distant clusters ($R \geq 7000$ km s$^{-1}$) of the Seven Samurai sample (Faber et al. 1989). A summary of the results and a discussion of the fitting technique adopted for the reduction of the photometric data of the EFAR project are given in Section 6. The Appendix provides a description of the numerical technique chosen in the computations.

## 2 SEEING CONVOLUTION: THE POINT SPREAD FUNCTION

### 2.1 The equations of seeing convolution

Astronomical images obtained with ground-based telescopes are degraded by seeing caused by atmospheric turbulence and by imperfections in telescope optics. We indicate the surface brightness distribution on the sky of an object by $I(\boldsymbol{R})$, where $\boldsymbol{R}$ is a two-dimensional vector denoting position on the sky; the integrated flux in an aperture of angular radius $R$ by $F(R) \equiv \int_0^R \int_0^{2\pi} R' \, dR' \, d\theta' I(\boldsymbol{R}')$; and the integrated magnitude within $R$ by $m(R) = -2.5 \log_{10} F(R)$. Given these definitions, the surface brightness distribution and the integrated flux recorded by an imaging instrument in the focal plane of a telescope are

$$I^c(\boldsymbol{R}) = \int_0^\infty \int_0^{2\pi} R' \, dR' \, d\theta' \, I(\boldsymbol{R}') p(\boldsymbol{R} - \boldsymbol{R}'), \quad (1)$$

$$F^c(R) = \int_0^R \int_0^{2\pi} R' \, dR' \, d\theta' I^c(\boldsymbol{R}'). \quad (2)$$

Accordingly, the convolved integrated magnitude within $R$ is $m^c(R) = -2.5 \log_{10} F^c(R)$. In equation (1), $p(\boldsymbol{R})$ is the point spread function of the observations, normalized so that $\int_0^\infty \int_0^{2\pi} p(\boldsymbol{R}) R \, dR \, d\theta = 1$. Equations (1) and (2) will be combined with model functions of the luminosity profile of elliptical galaxies in Section 4 to compute the effects of seeing on quantities that characterize these objects, such as $R_e$, $D_n$, $SB_e$ and $\langle SB_e \rangle$. In this section we discuss the choice of the point spread function, $p$.

Note that diffraction, guiding, focusing errors, bad alignment of the optics and charge transfer effects on the CCD can each cause non-circularly symmetric stellar profiles. Such observational problems can affect the ellipticity profiles of elliptical galaxies, depending on the ellipticity of the galaxy (see Peletier et al. 1990). The main goal of the present paper, however, is to evaluate the effects of seeing on the global parameters of elliptical galaxies, such as $D_n$, $R_e$, $SB_e$ and $\langle SB_e \rangle$, which in turn are typically derived from circularly averaged luminosity profiles. If a circularly averaged stellar profile is used to compute the effects of seeing on these quantities, only secondary effects are neglected by treating the psf itself as circular (see Franx et al. 1989). In the following we shall therefore ignore the actual deviations from circular symmetry of the point spread functions. We also choose to ignore sampling effects (Bendinelli, Parmeggiani & Zavatti 1987) due to the finite pixel size of the CCD detectors, as these may be important only in subarcsec seeing conditions.

### 2.2 The point spread function

Point spread functions can be determined observationally by studying the scattering of stellar light. Numerous papers, in

which both photographic and CCD detectors were used, have been devoted to this problem (e.g. Moffat 1969; King 1971; Bendinelli et al. 1984, 1987, 1988, 1990). Among the analytical approximations of the psf that are often used are Gaussian functions, Gaussian functions with exponential wings, and linear superpositions of Gaussian functions. The IRAF data reduction package (Tody 1986) adopts the Moffat (1969) function as a 'standard' psf:

$$p(R)=\frac{\beta-1}{\pi\alpha^2}\left[1+\left(\frac{R}{\alpha}\right)^2\right]^{-\beta}, \qquad (3)$$

with $\mathrm{FWHM}=2\alpha\sqrt{2^{1/\beta}-1}$, where $p(\mathrm{FWHM}/2)=(1/2)p(0)$ and the total flux is normalized to 1. A 'default' value of $\beta=2.5$ is suggested in the IRAF manual.

The theory of atmospheric turbulence predicts the psf to be the Fourier transform of $\exp[-(kb)^{5/3}]$ (Fried 1966; Woolf 1982), where $\mathrm{FWHM}=2.9207006b$ and $b$ is a scaling parameter. Here we consider a generalization of this functional form. We assume that the Fourier transform (see equation A1 in the Appendix) of the psf is

$$\hat{p}_\gamma(k)\equiv\int_0^\infty 2\pi R J_0(kR)p_\gamma(R)\,\mathrm{d}R=\exp[-(kb)^\gamma], \qquad (4)$$

with $1.3\leq\gamma\leq2$, and $J_0$ the standard Bessel function (see the Appendix). If $\gamma=2$, then $p_\gamma$ is a Gaussian. In Fig. 1 we plot both the Moffat and $p_\gamma$ functions for a range of $\beta$ and $\gamma$ values. Note that the Moffat functions do not approximate a Gaussian core as well as the $p_\gamma$ functions do.

We have checked the effect of the telescope diffraction patterns on the psf by convolving the $\gamma=5/3$ psf with the diffraction psf of a circular primary aperture blocked by a circular secondary (see Moffat 1969). We find that the effects are almost completely negligible for the 1 m class telescopes we have used [the 1.3-m Michigan–Dartmouth–MIT (MDM) Telescope and the 1-m J. Kapteyn Telescope (JKT)].

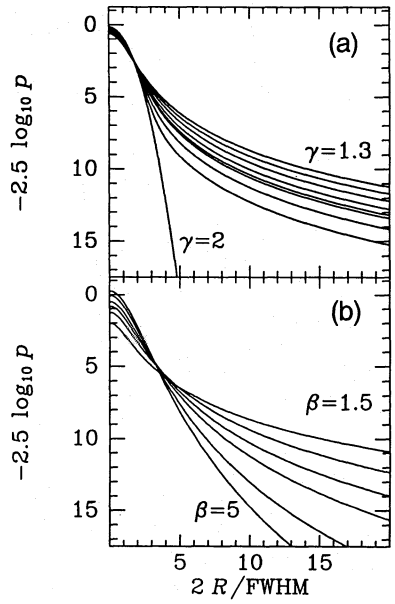


**Figure 1.** (a) The dimensionless surface brightnesses of the $p_\gamma$ psf functions (see equation 4) with $\gamma=1.3$, 1.4, ..., 2 and 5/3, plotted versus the radius of the psf in units of FWHM/2. (b) The analogous plot for the Moffat psf functions (see equation 3) with $\beta=1.5$, 2, 2.5, 3, 4 and 5.

### 2.3 Fits to stellar profiles

We have considered a number of randomly chosen CCD images taken at the Cassegrain focus of both the JKT and the 1.3-m MDM Telescope during photometric runs of the EFAR project (see Colless et al. 1993). With the JKT we used Mould $R$-band filters (Argyle et al. 1988) and GEC CCDs, with a pixel size of 0.3 arcsec and a field of $2.9\times1.9$ arcmin$^2$. The CCDs were binned $2\times2$ on chip. With the 1.3-m MDM Telescope we used an RCA CCD, with pixel size of 0.63 arcsec and a field of view of $5.4\times3.4$ arcmin$^2$, in combination with $R$-band Kron–Cousins filters (see Wegner et al. 1991). After standard reduction procedures (Colless et al. 1993), we derived from these images the luminosity profiles of 37 well-exposed, unsaturated stars, by computing the azimuthally averaged surface brightness with the GRASP software package (Cawson 1987). The stars were chosen to have peak intensities near 50 per cent of the CCD saturation value. This is well within the range in which the CCD is linear, and allows one to map the wings of the stellar profiles with a good signal-to-noise ratio. Thus the results discussed below are not biased by the particular choice of stellar profiles. The sky level is estimated as the mode of the pixel values in selected areas of the CCD frames. Some of these profiles are shown in Fig. 2.

We have fitted these profiles using the $p_\gamma$ and the Moffat psfs to determine the values of $\beta$ and $\gamma$ that produce the best fits. A least-squares fitting programme has been used to determine the FWHM, the total flux and the correction to the value of the sky level ($\Delta$ *SKY*). The programme is a simplified version of a code devised to fit galaxy profiles (Wegner et al. 1991; Bertschinger et al., in preparation). Two weighting schemes have been tested: equal weights (WS1) and weights (WS2) proportional to $I(R)/[I(R)+SKY]$, where $I(R)$ is the measured stellar surface brightness at $R$. The fits have been performed including all the data with $I/SKY\gtrsim0.01$–$0.05$.

The parameters derived from the fits are affected by the different weighting schemes and cut-off radii of the fits in different ways. The value of the FWHM is very robust and changes mainly because the best value of $\gamma$ (or of $\beta$) may happen to change. The best-fitting value of $\gamma$ is uncertain at most by one step of our grid ($\delta\gamma=0.1$). Fits performed with smaller cut-off radii or with lower weights to the outer parts (WS2) tend to give higher values of $\gamma$ because of the reduced influence of the wings of the stellar profiles. In these cases the correction to the sky values (typically $\pm2$ per cent) can sometimes increase to $\pm4$ per cent, and a smaller rms deviation is obtained because the noisy outer parts are not considered or have low weights. The best overall representation of the stellar profiles is obtained with WS2 and a cut-off at $I/SKY=0.01$. The results presented here have been derived using this choice of fitting parameters.

The reliability of the best-fitting values of the parameters FWHM, $\gamma$ and $\Delta SKY$ determined from the fit can be verified by comparing the results obtained from different star profiles derived from the same CCD frame. From the rms deviations of fits to different stars observed under the same

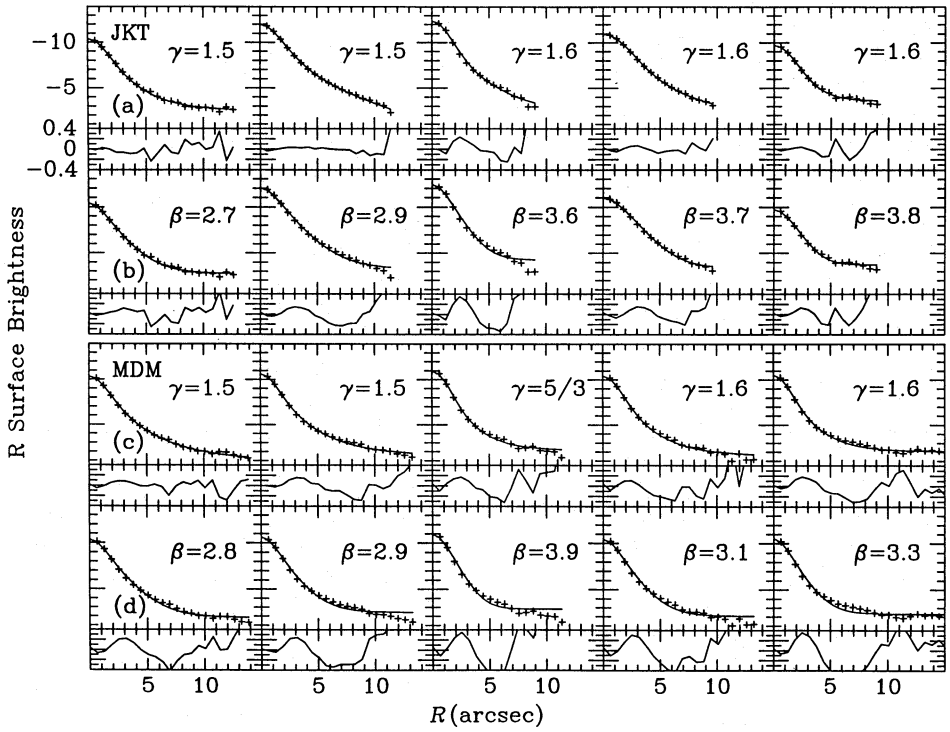


**Figure 2.** Row (a): $-2.5\log_{10}$ counts arcsec$^{-2}$ (in the $R$ band) for five stellar profiles measured with the JKT (crosses). The full lines show the best fits obtained with the $p_\gamma$ psf; the value of $\gamma$ is also given. The residuals from these fits (model data) are shown below. Row (b): we show the best fits and the corresponding residuals obtained with the Moffat function (the values of $\beta$ are now given) for the same stars as in row (a). Rows (c) and (d) are as (a) and (b) for stars observed with the MDM Telescope.

conditions, we estimate that FWHM is determined to better than 0.1 arcsec, $\gamma$ to better than one step of our grid ($\delta\gamma \leq 0.1$), and the sky value to better than 1 per cent.

The results of the fits are shown in detail for 10 stellar profiles in Fig. 2. Note that the fitted lines incorporate the correction for the sky value. Both the $p_\gamma$ function and Moffat's functions are able to reproduce the overall behaviour of the observed stellar profiles over a range of up to 9 mag, with residuals typically less than 0.2 mag arcsec$^{-1}$. The Moffat function, however, tends to give systematically lower luminosities than the data in the inner parts ($R \approx 2$ arcsec) and higher luminosities than the data at larger radii ($R \approx 6$ arcsec). This systematic trend is much less pronounced when the $p_\gamma$ fits are considered. Note also that the best fits with Moffat functions tend to be obtained for values of $\beta$ larger than 2.5, the value implemented as a default by IRAF.

Fig. 3 shows histograms of the ratios of the rms deviations of the best fits obtained with the $p_\gamma$ function to those obtained with Moffat function for the 37 stellar profiles we have analysed. In all cases except one, the $p_\gamma$ functions yield the smaller residuals. We therefore conclude that the $p_\gamma$ family gives a superior analytical approximation of the stellar profiles measured with the 1.3-m MDM Telescope and the JKT. Consequently, the results described in Section 4 are derived using this form of psf.

Previous studies of the analytical approximation of stellar profiles (Bendinelli et al. 1987, 1988, 1990) concluded that Moffat and multi-Gaussian approximations give statistically equally good fits, with residuals $\lesssim 0.125$ mag arcsec$^{-2}$. Here we have shown that the $p_\gamma$ family gives fits as good as, or

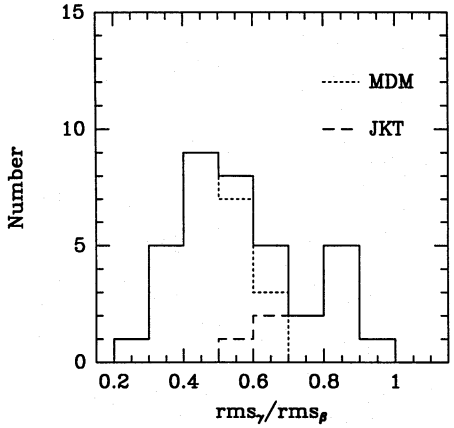


**Figure 3.** Histograms of the ratios between the residuals rms$_\gamma$ and rms$_\beta$ of the best fits obtained using the $p_\gamma$ psf and the Moffat functions to stellar profiles measured with the JKT (long-dashed line) and the MDM Telescope (short-dashed line). The full line shows the sum of the two. The $p_\gamma$ psf gives smaller residuals in all but one case.

better than, those based on the Moffat function. With respect to the multi-Gaussian approach, the $p_\gamma$ family has fewer free parameters and a clearer physical interpretation (values of $\gamma \approx 5/3$ correspond to the predictions of the standard model of atmospheric turbulence). In fact, the values of $\gamma$ that produce the best fits are in the range 1.5–1.7 (see Figs 4a and b), in reasonably good agreement with this theoretical value. In general, the values of $\gamma$ that give the best representation of

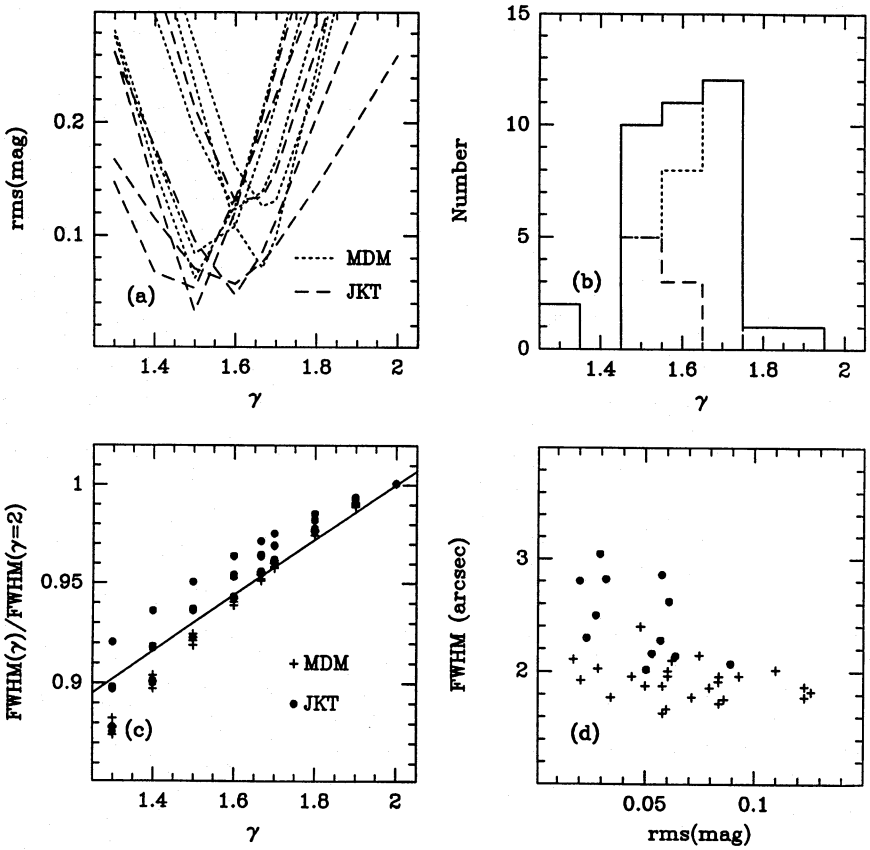


**Figure 4.** (a) Residuals of the fits to the JKT (long-dashed lines) and to the MDM Telescope (short-dashed lines) stellar profiles as a function of the psf parameter $\gamma$. (b) Histograms of the best-fitting values of $\gamma$ derived for JKT stars (long-dashed line) and for MDM stars (short-dashed line). The full line shows the sum of the two. (c) The ratio FWHM($\gamma$)/FWHM($\gamma=2$) obtained from the fits to JKT stars (filled circles) and to MDM stars (crosses) as a function of $\gamma$. The full line shows the relation of equation 5. (d) The values of the FWHM (in arcsec) derived from the best fits to JKT stars (filled circles) and to MDM stars (crosses) as a function of the rms of the fits. Note that the quality of the fit is independent of FWHM.

the stellar profiles observed with a given telescope may depend on the specific set-up, and therefore may differ from $\gamma=5/3$. They should be determined for each case separately.

Values of FWHM quoted by observers are often derived from single Gaussian fits to the cores of stellar profiles. Fig. 4(c) shows how to translate a Gaussian FWHM into a $p_\gamma$ model FWHM. This is a necessary step for observers willing to correct their raw $R_e$, $D_n$ and surface brightness values using Figs 8 and 9 (see later). The following relation holds:

$$\frac{\mathrm{FWHM}(\gamma)}{\mathrm{FWHM}(\gamma=2)}=1-0.14(2-\gamma). \qquad (5)$$

This relation has been derived by fitting a Gaussian to the $p_\gamma$ psf and using an equal-weight fit which is based on the logarithm of the surface brightness and which includes data out to 2 FWHM. The coefficient $-0.14$ becomes $-0.19$ if data out to 2.5 FWHM are considered. Fig. 4(c) shows equation 5 together with the values of the ratio FWHM($\gamma$)/FWHM($\gamma=2$) obtained from the fits to different stars. Gaussian fits to observed psfs overestimate the seeing value because they are not able to follow the outer wings.

No correlation is found between the derived FWHM and the residuals of the best fit (Fig. 4d). The $p_\gamma$ family represents equally well stellar profiles taken in good and bad seeing conditions and stellar profiles measured both with the 1.3-m MDM Telescope and with the JKT.

## 3 MODELS OF THE LIGHT DISTRIBUTION OF ELLIPTICAL GALAXIES

Elliptical galaxies are three-dimensional stellar systems. Studies of their surface brightness distributions have shown that their isophotes are well represented by concentric ellipses, within which the ellipticity and position angle of the major axis can vary with distance from the centre (e.g. Carter 1978). Deviations from pure ellipses have also been measured, leading to an important distinction between boxy and disky ellipticals (Bender & Möllenhoff 1987). However, the global dimensional quantities of elliptical galaxies, such as $R_e$ and $D_n$, are derived from circularly averaged profiles. When averaged over the azimuthal angle or plotted in terms of the circularized distance from the centre $R=\sqrt{ab}$, where $a$ and $b$ are the semimajor and semiminor axes of the isophotes, the surface brightness distribution $I(R)$ follows the $R^{1/4}$ law

$$I_{1/4}(R)=I_e\exp\{-7.67[(R/R_e)^{1/4}-1]\} \qquad (6)$$

(de Vaucouleurs 1948). The integrated flux inside an aperture of radius $R$ is given by

$$F_{1/4}(R)=\int_0^R 2\pi R' I_{1/4}(R')\,\mathrm{d}R', \tag{7}$$

$$F_{1/4}(\infty)=7.22\pi R_e^2 I_e. \tag{8}$$

In equations (6) and (7), $R_e$ is the half-luminosity radius, at which $F_{1/4}(R_e)=0.5F_{1/4}(\infty)$, and $I_e$ is the surface brightness at $R_e$. Note that in this case $SB_e=-2.5\log_{10}I_e$ and $\langle SB_e\rangle=-2.5\log_{10}[F_{1/4}(R_e)/\pi R_e^2]$.

Equation (6) is a very good representation of the luminosity profile of elliptical galaxies. Typical observed deviations are smaller than 0.1 mag arcsec$^{-2}$ in the radial range 0.1–4 $R_e$. Larger deviations are sometimes present at smaller and larger radii (see Bertschinger et al., in preparation). In order to explore the possible range of seeing effects it is therefore important to consider both kinds of deviation.

Previous studies of the effects of seeing on the light distribution in the cores of ellipticals (Schweizer 1979; Lauer 1985; Kormendy & Richstone 1992) have adopted the $R^{1/4}$ profile, as well as the less centrally concentrated King (1966) models, in order to explore the range of the effects. We have considered three forms of luminosity profile, including the $R^{1/4}$ law as well as a model that is more centrally concentrated and one that is less so. The less centrally concentrated model was obtained by convolving the $R^{1/4}$ law with a Gaussian of FWHM $=0.04R_e$. In the following we shall refer to this as the 'smoothed model'.

The more centrally concentrated model is given by the $\Psi=12$ self-consistent $f_\infty$ model (Bertin & Stiavelli 1984; Stiavelli & Bertin 1985). In the spherical limit, the $f_\infty$ stellar distribution function is defined as

$$f_\infty=A(-E)^{3/2}\exp(-aE-cJ^2/2), \tag{9}$$

where $E=v^2/2+\Phi\leq 0$ is the energy per unit mass, $\Phi$ is the gravitational potential, $J$ is the specific angular momentum, and $A$, $a$ and $c$ are constants. The $f_\infty$ function, which describes the final state of dissipationless collapse, produces an isotropic pressure tensor for $R\lesssim R_e$ and a radial pressure tensor in the outer parts. When the gravitational potential is determined self-consistently by integrating the Poisson equation, equation (9) describes a one-parameter equilibrium sequence. A self-consistent $f_\infty$ model is specified by fixing two-dimensional length-scales (such as the total mass and the half-mass radius) and the value of the dimensionless central potential $\Psi=-a\Phi(0)$. For large values of $\Psi$ ($\Psi\gtrsim 7.7$) the projected density of the $f_\infty$ models gives good fits to the photometry of bright elliptical galaxies assuming a constant mass-to-light ratio (Bertin, Saglia & Stiavelli 1988). The $\Psi=12$ model has a higher central surface density than the $R^{1/4}$ law, and falls less steeply ($\propto R^{-3}$) than the $R^{1/4}$ law in the outer parts. The surface density and integrated flux profiles of the $\Psi=12$ models have been computed numerically following Stiavelli & Bertin (1985), with an estimated precision of 0.01 per cent.

Surface brightness and integrated flux profiles for the $R^{1/4}$ model, the smoothed model and the $\Psi=12$ model are plotted in Fig. 5 as a function of $(R/R_e)^{1/4}$ and normalized to a total flux of 1. These three models roughly cover the possible overall variations of the luminosity profiles of ellipticals. Note, however, that a detailed discussion of the light distribution in the very central regions of ellipticals (and the issue of central black holes; see Lauer et al. 1992) is beyond the scope of this paper.

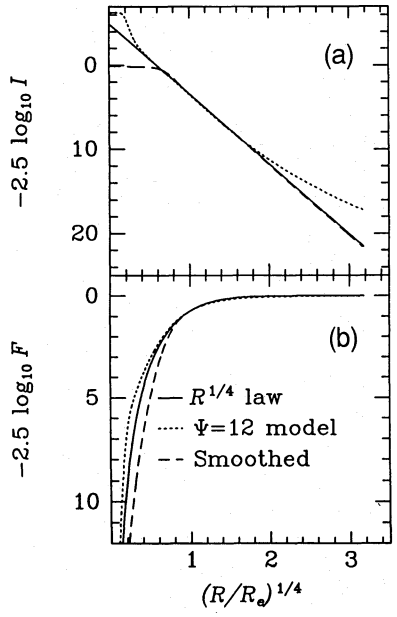


**Figure 5.** (a) The surface brightness profiles of the $R^{1/4}$ law (full line), the smoothed model (long-dashed) and $\Psi=12$ model (short-dashed) as a function of the 1/4 power of the projected radius normalized to $R_e$. (b) The flux (in magnitudes) integrated in circular apertures is shown for the same models with the same notation.

## 4 THE EFFECTS OF SEEING ON THE PHOTOMETRIC PROPERTIES OF ELLIPTICAL GALAXIES

In this section the results of the numerical seeing convolutions beween the $p_\gamma$ psfs (see equation 4) and the three models described in the previous section are presented. The numerical methods used to compute equations (1) and (2) are described in the Appendix.

### 4.1 Surface brightness

The effects of seeing on the surface brightness profiles are shown in Fig. 6. Here the logarithm of the ratio $I^c/I$ between the surface brightness convolved with the $p_\gamma$ psfs and the original profiles of the three models of Fig. 5(a) is plotted for a range of values of the ratio FWHM/$2R_e$. For small values of FWHM/$2R_e$ (i.e. large galaxies or good seeing), seeing effects are negligible for $R\gtrsim 5$ FWHM. Because seeing spreads light from the centre outwards, the convolved surface brightness is lower than the original one for $R\lesssim$ FWHM and higher at larger radii. The ratio $I^c/I$ has a maximum at $R/\mathrm{FWHM}\approx 1.3$. Seeing effects are more extensive for the lower $\gamma$ psfs, which is expected as they have broader wings (see Fig. 1).

All three luminosity profile models show the same qualitative behaviour with respect to seeing convolution. However, at small radii and at small values of FWHM/$2R_e$, the

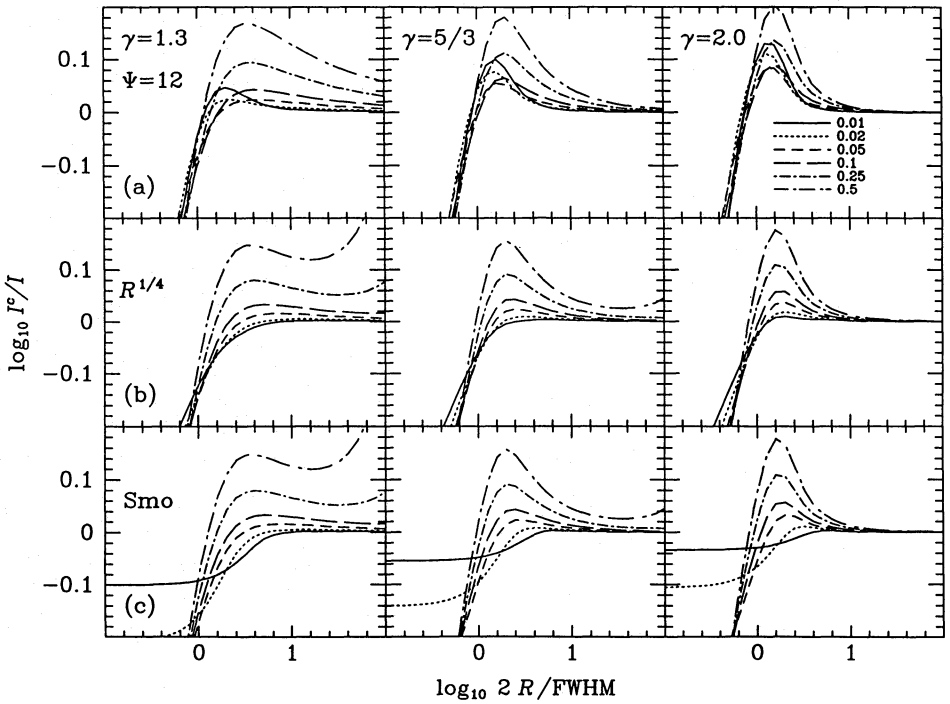


**Figure 6.** Row (a): the logarithm of the ratio of the seeing-convolved surface brightness to the original profile for the $\Psi = 12$ model plotted versus the logarithm of the radius in units of FWHM/2 for three values of $\gamma$ [1.3: left-hand panels; 5/3: middle panels; 2.0 (Gaussian psf): right-hand panels] and for six values of the ratio FWHM/$2R_e$ (0.01, 0.02, 0.05,0.1, 0.25 and 0.5). Rows (b) and (c): the same quantity is plotted for the $R^{1/4}$ law (b) and for the smoothed model (c) (see Section 4.1).

presence of the central concentration of the $\Psi = 12$ model is apparent. At very large radii in the $R^{1/4}$ and smoothed models, the ratio $I^c/I$ starts to increase, whilst in the $\Psi = 12$ model $I^c/I \rightarrow 1$. This is due to the fact that the projected density of the $\Psi = 12$ model falls as $R^{-3}$ at large radii, while the $R^{1/4}$ profile declines exponentially, in particular more rapidly than the $p_\gamma$ profiles. In the latter case, scattered light from the centre dominates the underlying $R^{1/4}$ profile and the convolved profile follows the psf profile at large radii. However, the effect is seen only at $R \geq 10R_e$, and should be irrelevant in all practical cases.

### 4.2 Integrated flux

Fig. 7 shows the differences in magnitudes $\Delta m(R) = m^c(R) - m(R)$ between the convolved integrated fluxes in circular apertures and the original ones, for the same set of models and psfs as in Fig. 6. Fluxes of convolved models are always smaller than the original fluxes, because light is scattered from the centre outwards. A typical 1-mag 'dimming' occurs at one seeing radius (FWHM/2). As in the case of the convolved surface brightness, large effects are caused by low-$\gamma$ psfs. Note that the variation of FWHM/$2R_e$ has the least effect on $\Delta m$ for the $\Psi = 12$ model and the largest effect for the smoothed $R^{1/4}$ law. In the former case, light scattered from the central cusp dominates the profile and this contribution is independent of $R_e$. In the latter case, light scattered from the centre is less important, due to the flatter core of the model, and consequently the effect of variations in FWHM/$2R_e$ is more pronounced.

### 4.3 Half-luminosity radius $R_e$ and effective surface brightness $\langle SB_e \rangle$ and $SB_e$

Due to the dimming of aperture magnitudes, the half-luminosity radius $R_e^c$ derived from a seeing-convolved profile is always larger than the true value $R_e$. In Fig. 8(a) the relation between $R_e/R_e^c$ and $R_e^c$/FWHM is shown for the three models and for three values of $\gamma$. Measured values of $R_e^c$ greater than 10 FWHM overestimate $R_e$ by no more than 2.5 per cent for $\gamma \geq 1.4$. The mean surface brightness inside $R_e^c$, $\langle SB_e^c \rangle$, is lower than the true value. In fact, since the total luminosity of a galaxy is not changed by the seeing, it follows from the definition of mean surface brightness that

$$\Delta\langle SB_e \rangle = \langle SB_e^c \rangle - \langle SB_e \rangle = +5 \log_{10} \frac{R_e^c}{R_e}. \quad (10)$$

If $R_e^c > 10$ FWHM, the derived mean effective surface brightnesses are fainter than the true values by no more than 0.05 mag arcsec$^{-2}$.

Finally, Fig. 8(b) shows the relation between $R_e^c$/FWHM and $\Delta SB_e$:

$$\Delta SB_e = SB_e^c - SB_e = -2.5 \log_{10} \frac{I^c(R_e^c)}{I(R_e)}. \quad (11)$$

Note that $\Delta SB_e$ is smaller than $\Delta\langle SB_e \rangle$ at any given value of $R_e^c$/FWHM. In fact, $\Delta SB_e$ can be seen as the sum of two terms, $-2.5 \log_{10}[I(R_e^c)/I(R_e)]$ and $-2.5 \log_{10}[I^c(R_e^c)/I(R_e^c)]$. The first one is positive, because $R_e^c > R_e$ and

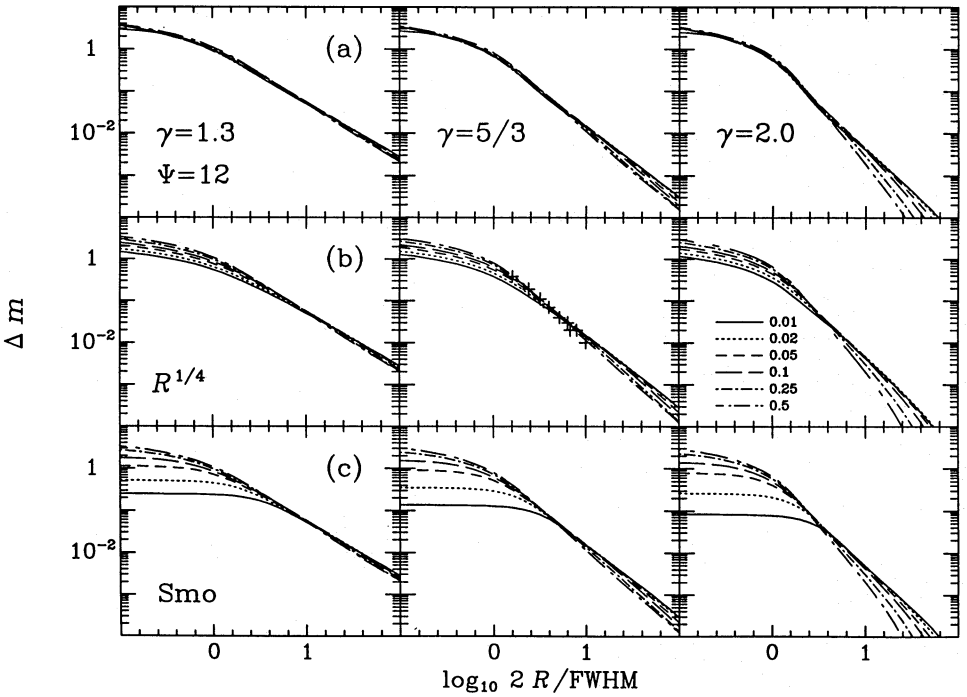


**Figure 7.** Row (a): the differences between the integrated magnitudes in circular apertures of the seeing-convolved and original $\Psi = 12$ models, $\Delta m(<R)$, are plotted as a function of the logarithm of the radius in units of FWHM/2 for three values of $\gamma$ (1.3: left-hand panel; 5/3: middle panel; 2.0: right-hand panel) and for six values of the ratio FWHM/$2R_e$ (0.01, 0.02, 0.05, 0.1, 0.25 and 0.5). Rows (b) and (c): the same quantity is plotted for the $R^{1/4}$ law (b) and for the smoothed model (c) (see Section 4.2). Crosses in the central panel of row (b) show Lucey's corrections (see Section 4.7) for FWHM/$2R_e = 0.25$.

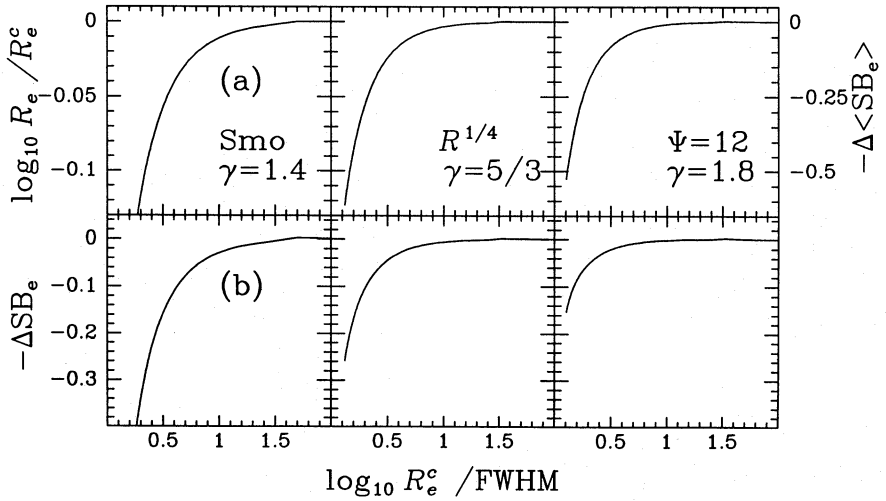


**Figure 8.** Corrections to the seeing-convolved effective radius $R_e^c$, mean effective surface brightness $\langle SB_e^c\rangle$, and effective surface brightness $SB_e^c$. Row (a), middle panel: the relation between $R_e/R_e^c$ and $R_e^c$/FWHM. The curves have been computed for the $R^{1/4}$ model and with $\gamma = 5/3$. Use this plot in combination with equation (5) to derive seeing corrections to $R_e^c$. The scale on the right gives the correction to be added to $\langle SB_e^c\rangle$ values (see equation 10). Row (b), middle panel: the correction to be added to raw $SB_e^c$ values. Left- and right-hand panels: the same quantities are shown for the smoothed model with $\gamma = 1.4$ and for the $\Psi = 12$ model with $\gamma = 1.8$. Use these plots to derive the possible range of seeing corrections (see Section 4.6).

$I$ is decreasing, and approximately equal to

$$8.325\left[\left(\frac{R_e^c}{R_e}\right)^{1/4} - 1\right] \approx \frac{8.325}{4}\left(\frac{R_e^c}{R_e}\right) \approx 0.4\Delta\langle SB_e\rangle \qquad (12)$$

(see equation 10). The second term, $2.5\log_{10}[I^c(R_e^c)/I(R_e^c)]$, is negative for $R_e^c$/FWHM $\gtrsim 1$ (see Fig. 6). For $R_e^c$/FWHM $\gtrsim 40$ this second term becomes dominant for the $R^{1/4}$-based models and $\Delta SB_e < 0$.

### 4.4 $D_n$ diameters

An effect similar to that discussed above, but in the opposite direction, is observed for $D_n$. $D_n$ is defined as the diameter of

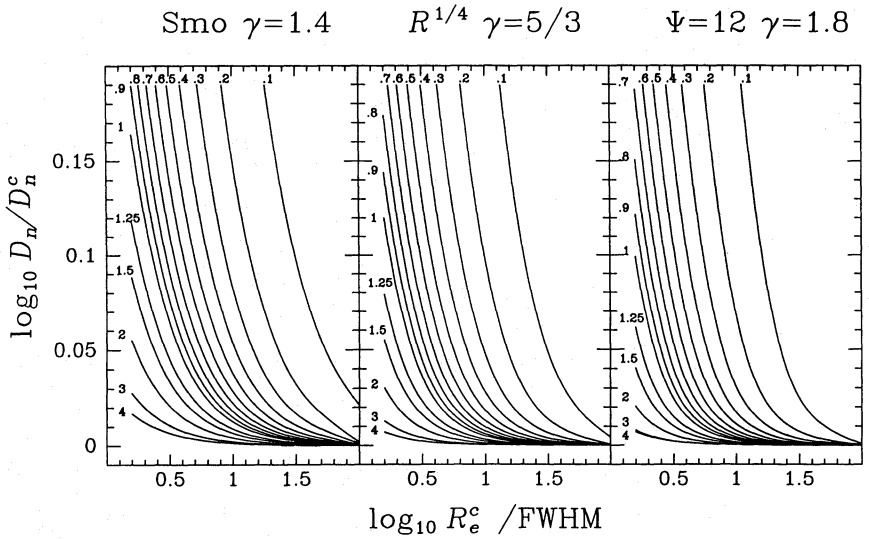


**Figure 9.** Corrections to the seeing-convolved diameter, $D_n^c$. Middle panel: the relation between $D_n/D_n^c$ and $R_e^c$/FWHM at constant $D_n^c/R_e^c$ ratios (indicated on the curves). The curves have been computed for the $R^{1/4}$ model and with $\gamma = 5/3$. Use this plot in combination with equation (5) to derive seeing corrections to $D_n^c$ values. Left and right panels: the same quantities are shown for the smoothed model with $\gamma = 1.4$ and for the $\Psi = 12$ model with $\gamma = 1.8$. Use these plots to derive the possible range of seeing corrections (see Section 4.6).

an aperture enclosing a fixed mean surface brightness: $F = \pi(D_n/2)^2\langle I_0\rangle$. Because seeing always decreases the integrated flux (Fig. 7), the $D_n^c$ derived from a seeing-convolved profile is always smaller than the true value. As can be seen from Fig. 9, the ratio $D_n^c/D_n$ decreases as $R_e$ decreases. For large $R_e$ or for large values of $D_n/R_e$ (i.e. choosing a fainter surface brightness level $\langle I_0\rangle$ to compute $D_n$), the seeing convolution has little effect on $D_n$ as $D_n^c/D_n \rightarrow 1$. At sufficiently small $R_e$ the mean surface brightness of the convolved profile becomes lower than the value adopted to compute $D_n$, and so $D_n^c = 0$. Low values of $\gamma$ produce the largest effects on $D_n^c$. The effects of seeing are somewhat larger in the $R^{1/4}$-law and the smoothed $R^{1/4}$ cases.

### 4.5 The $D_n$–$\sigma$ relation and the fundamental plane

The distances of ellipticals can be predicted from either the $D_n$–$\sigma$ relation (Faber et al. 1989) or from the values of $R_e$, $SB_e$(or $\langle SB_e\rangle$) and $\sigma$ that define the fundamental plane for ellipticals (e.g. Djorgovski & Davis 1987; Jørgensen, Franx & Kjærgaard 1992).

Seeing effects bend the relation at small $D_n^c$, with the net result of producing a shallower relation, increasing the scatter, and shifting the zero-point to higher values. As a consequence, distances derived from uncorrected $D_n$–$\sigma$ data are higher than the true values and produce spurious negative 'peculiar velocities'. The size of the effect is proportional to the number of objects in the lower end of the $D_n$–$\sigma$ relation, so that well-sampled distant clusters are more strongly affected by seeing.

The effects of seeing on the fundamental plane are completely equivalent to those for the $D_n$–$\sigma$ relation. When one plots $\log_{10} R_e$ versus $1.3\log_{10}\sigma + 0.35\langle SB_e\rangle$ (Faber et al. 1987), seeing effects move points above the relation due to equation (10). As before, a shallower relation is derived, the scatter is increased, and the zero-point is shifted to a higher value.

### 4.6 A prescription for seeing corrections

The central plots of Figs 8 and 9 give the corrections to be applied to raw $R_e^c$, $\langle SB_e^c\rangle$, $SB_e^c$ and $D_n^c$ values to obtain seeing-free quantities. These relations must be used in combination with equation (5). The central plots are computed for the $R^{1/4}$ law with $\gamma = 5/3$. The plots to the right and to the left are computed for the smoothed model with $\gamma = 1.4$, and for the $\Psi = 12$ model with $\gamma = 1.8$, respectively. They show the maximum and the minimum variations of the corrections displayed in the central plots that one expects from the possible range in $\gamma$ (see Fig. 4) and for the different choices of galaxy models.

The relation between $R_e/R_e^c$ and $R_e^c$/FWHM is shown in row (a) of Fig. 8. Once $R_e/R_e^c$ is determined, the correction to be added to raw mean effective surface brightnesses $\langle SB_e^c\rangle$ to eliminate seeing effects is $5\log_{10}(R_e/R_e^c)$ (see equation 10). Row (b) of Fig. 8 gives the corrections to be added to raw effective surface brightnesses $SB_e^c$. Fig. 9 shows the lines of constant $D_n^c/R_e^c$ ratio as a function of $R_e^c$/FWHM and of $D_n/D_n^c$.

In summary, observers should:

(1) determine the FWHM of stars by fitting a Gaussian;

(2) use equation (5) to transform this width to that appropriate to the range of $\gamma$ observed with their telescope set-up (for all non-pathological cases this should correspond to that shown in Figs 8 and 9);

(3) determine the corrections to $R_e$, $\langle SB_e\rangle$, $SB_e$ and $D_n$ from the figures.

### 4.7 The seeing corrections of Lucey et al.

Lucey et al. (1991a) adopted a different method to derive the seeing-corrected values of $D_n$ and $R_e$ for galaxies of a given (distant) cluster. They first computed the effects of seeing on the integrated fluxes inside circular apertures for an $R^{1/4}$ law, using the combined modulation function of the telescope and

atmosphere. A *fixed* value of $R_e$, typical for the galaxies of the cluster under study (e.g. $R_e = 5$ arcsec for the Coma and A2634 clusters; see Lucey et al. 1991a), is chosen. These corrections are then applied to all the observed aperture magnitudes (independently of the actual value of $R_e$ for a galaxy) before deriving the $R_e$ and $D_n$ values. Such corrections (taken from table 6b of Bower et al. 1992) are shown as crosses in Fig. 7 for the case $\mathrm{FWHM}/2R_e = 0.25$. They are equivalent (for the given numerical accuracy of the table, $\approx 0.01$ mag) to our tables computed for the $R^{1/4}$ model and with $\gamma = 5/3$. For simplicity, therefore, these tables have been used to perform the tests described below, setting $\mathrm{FWHM}/2R_e = 0.15$ (i.e. using the average seeing of FWHM = 1.5 arcsec quoted by Lucey et al. 1991a and $R_e = 5$ arcsec).

Using the method of Lucey et al., we find that corrected $R_e$ and $D_n$ values can differ from the true ones due to three effects: (a) the galaxy has a value of $R_e$ different from that assumed to compute the corrections; (b) the galaxy has a core more or less concentrated than the $R^{1/4}$ law; and (c) the real psf has $\gamma > 5/3$ or $\gamma < 5/3$.

The lines of Fig. 10(a) show the relation between the values $R_e^L$ of the half-luminosity radius (normalized to the true values) derived after applying the corrections of Lucey et al. and the true values (in units of FWHM). The main effect visible here is (c) above: the derived $R_e^L$ appears to be overcorrected (smaller than the true values) for $\gamma > 5/3$, and undercorrected for $\gamma < 5/3$. Effect (b) causes the derived $R_e^L$ of the smoothed model with $\gamma = 5/3$ to underestimate slightly the true values, because the aperture magnitudes have been overcorrected. Effect (a) causes the derived $R_e^L$ of the $R^{1/4}$ model with $\gamma = 5/3$ to overestimate the true values for $\mathrm{FWHM}/2R_e > 0.15$ (because the applied corrections to aperture magnitudes underestimate the true values), but the effect is too small to be visible in the figure.

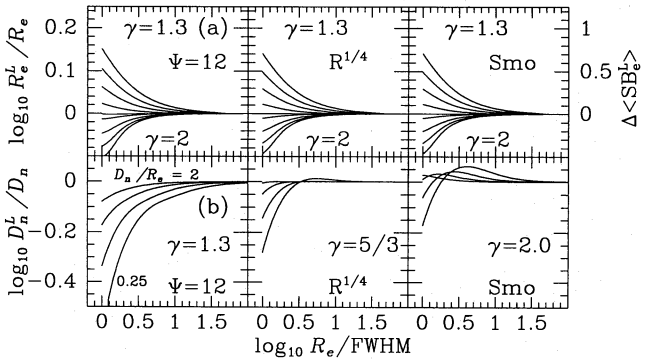


**Figure 10.** (a): Lucey's corrections to $R_e$. The relation between the logarithm of the ratio $R_e^L/R_e$ and $R_e$/FWHM for the $\Psi = 12$ model (left), the $R^{1/4}$ profile (middle), and the smoothed model (right), for a range of $\gamma$ values (from 1.3 to 2) is shown. The half-luminosity radius $R_e^L$ is derived by applying Lucey's method (see Section 4.7). Radii derived using Lucey's method are undercorrected for $\gamma < 5/3$ ($R_e^L/R_e > 1$) and overcorrected for $\gamma > 5/3$. The scale on the right shows the corresponding variations of the mean effective surface brightness (see equation 10). (b) Lucey's corrections to $D_n$. In each box ($\gamma = 1.3$ and the $\Psi = 12$ model on the left, $\gamma = 5/3$ and the $R^{1/4}$ model in the middle, and $\gamma = 2.0$ and the smoothed model on the right), four curves are shown. These (obtained for $D_n/R_e = 2$, 1, 0.5 and 0.25) give the relation between $D_n^L/D_n$ and $R_e$/FWHM when $D_n^L$ is computed using Lucey's method. Lucey's method undercorrects $D_n$ for $\gamma = 1.3$ ($D_n^L/D_n < 1$) and overcorrects it for $\mathrm{FWHM}/2R_e < 0.15$ and $\gamma = 5/3$ or for $\gamma = 2$ (see Section 4.7 for a detailed discussion).

Fig. 10(b) shows the values of $D_n$ corrected by the method of Lucey et al., i.e. $D_n^L$, as a function of $R_e$. Again, the most prominent effect is (c): for $\gamma = 1.3$, the $D_n^L$ values are always smaller than the true values, while for $\gamma = 2$ they appear larger than the true values at large $R_e$. Effect (a) causes the $D_n^L$ derived for the $R^{1/4}$ model with $\gamma = 5/3$ to underestimate the true values for $\mathrm{FWHM}/2R_e > 0.15$ (because the applied corrections to aperture magnitudes underestimate the true values), and to overestimate the true $D_n$ for smaller $\mathrm{FWHM}/2R_e$ ratios. Effect (b) reduces effect (a) in the case of the more centrally concentrated $\Psi = 12$ model (because the aperture corrections depend less on $\mathrm{FWHM}/2R_e$; see Fig. 7). Of course, we note from Fig. 4 that $\gamma$ is typically close to 5/3.

Finally, if $D_n^L$ values are used in the $D_n$–$\sigma$ relation, the residual errors in the distances are small and deviations from the reference line are appreciable only for extreme (and unrealistic) values of $\gamma$ (due to effect c). The relation appears shallower than the true one for $\gamma = 1.3$ (since $D_n^L$ values are undercorrected) and steeper than the true one if $\gamma = 2$ (since $D_n^L$ values are overcorrected due to effects a and c). An estimate of the size of these residual (small) effects is given at the end of the next section for the case of elliptical galaxies in the cluster Abell 2634.

## 5 THE DISTANT CLUSTERS OF THE SEVEN SAMURAI SAMPLE

Abell 2199 is the most distant well-sampled cluster studied by the Seven Samurai, and also has the largest negative peculiar velocity of any cluster in their list, $\Delta v = -2919$ km s$^{-1}$ (Faber et al. 1989). In addition, all galaxies and clusters at distances greater than 7000 km s$^{-1}$ (columns 8 of table 4, in Faber et al. 1989) have quite high negative peculiar velocities, with the exception of Abell 2634. In Table 1 a list of such objects is given.

The great majority of the ellipticals in the Faber et al. (1989) list have effective radii larger than 20 arcsec. In addition, most of the photometry comes from photoelectric measurements, where seeing information was not recorded.

**Table 1.** The distant clusters of the Faber et al. (1989) sample, from their table 4.

| Name | $N_{Gr}$ | $N_{obs}$ | $R$ (km s$^{-1}$) | $\Delta v_{raw}$ (km s$^{-1}$) |
|---|---|---|---|---|
| A569 | 36 | 5 | 6954 | -1123 |
| GH130 | 227 | 1 | 7091 | -1022 |
| GH90 | 51 | 5 | 7171 | -513 |
| | 277 | 1 | 7516 | 40 |
| Coma | 61 | 21 | 7461 | -258 |
| A779 | 41 | 3 | 7866 | -804 |
| NGC 80 | 21 | 2 | 7945 | -2611 |
| | 89 | 2 | 8184 | -219 |
| | 23 | 2 | 8393 | -653 |
| DC2345-28 | 72 | 10 | 9134 | -565 |
| A2634 | 251 | 1 | 8637 | 425 |
| | 104 | 2 | 9468 | -331 |
| E115-G008 | 272 | 1 | 11060 | -1914 |
| A2162 | 233 | 1 | 11510 | -1885 |
| A2199 | 73 | 11 | 11918 | -2919 |

No seeing correction has therefore been applied to these data. Here we want to investigate how large the influence of seeing could have been, in relation to the large negative peculiar velocities found for the distant clusters of the sample. In the following we assume an average seeing value of FWHM = 2 arcsec. The observed and seeing-corrected values of $R_e$, $D_n$ and $\langle SB_e \rangle$ (derived using Figs 8 and 9) for the galaxies in two representative clusters, A2199 and DC 2345 − 28, are given in Table 2. The corrections applied for one small object with $R_e$/FWHM < 1 have been computed assuming $R_e$/FWHM = 1. The possible range of the corrections is also given.

Fig. 11 shows the $D_n$–$\sigma$ plots for these two distant clusters, together with the comparison plot obtained for Coma. Large galaxies are only marginally affected by seeing, but smaller objects are systematically shifted towards larger $D_n$s by seeing corrections. The zero-point shift between the observed and seeing-corrected $D_n$–$\sigma$ relations can be

**Table 2.** Seeing-corrected (see text) values of $R_e$, $D_n$ and $\langle SB_e \rangle$ for the galaxies of the DC 2345 − 28 and A2199 clusters. Observed values are taken from Faber et al. (1989). The range of the corrections is also given.

| Galaxy | $R_e^c$ (″) | $D_n^c$ (″) | $\langle SB_e^c \rangle$ mag arcsec$^{-2}$ | $R_e$ (″) | $D_n$ (″) | $\langle SB_e \rangle$ mag arcsec$^{-2}$ | $(\Delta v)_{seeing}$ (km s$^{-1}$) |
|---|---|---|---|---|---|---|---|
| DC2345-28 | | | | | | | $-577^{+145}_{-340}$ |
| DC23-032 | 7.5 | 12.5 | 21.20 | $7.2^{+0.1}_{-0.4}$ | $12.8^{+0.4}_{-0.1}$ | $21.11^{+0.03}_{-0.13}$ | |
| DC23-042 | 43.4 | 9.7 | 23.64 | $43.3^{+0.1}_{-0.3}$ | $10.2^{+0.6}_{-0.2}$ | $23.64^{+0.00}_{-0.01}$ | |
| DC23-044 | 1.6 | 5.9 | 19.93 | $1.2^{+0.1}_{-0.2}$ | $6.0^{+0.1}_{-0.1}$ | $19.32^{+0.09}_{-0.30}$ | |
| DC23-045 | 4.9 | 9.7 | 21.49 | $4.5^{+0.1}_{-0.5}$ | $10.1^{+0.4}_{-0.1}$ | $21.30^{+0.06}_{-0.24}$ | |
| DC23-052 | 4.3 | 3.1 | 22.31 | $3.9^{+0.1}_{-0.5}$ | $4.2^{+0.5}_{-0.2}$ | $22.07^{+0.07}_{-0.28}$ | |
| DC23-054 | 4.8 | 6.0 | 21.59 | $4.3^{+0.1}_{-0.5}$ | $6.5^{+0.4}_{-0.2}$ | $21.39^{+0.06}_{-0.24}$ | |
| DC23-055 | 5.0 | 8.3 | 21.19 | $4.6^{+0.1}_{-0.5}$ | $8.7^{+0.4}_{-0.1}$ | $21.00^{+0.06}_{-0.23}$ | |
| DC23-056 | 16.9 | 14.7 | 22.07 | $16.7^{+0.1}_{-0.4}$ | $15.0^{+0.4}_{-0.1}$ | $22.05^{+0.01}_{-0.05}$ | |
| DC23-058 | 5.7 | 10.0 | 21.09 | $5.3^{+0.1}_{-0.5}$ | $10.3^{+0.4}_{-0.1}$ | $20.94^{+0.05}_{-0.19}$ | |
| DC23-060 | 4.0 | 7.0 | 21.12 | $3.6^{+0.1}_{-0.5}$ | $7.5^{+0.4}_{-0.1}$ | $20.85^{+0.08}_{-0.30}$ | |
| DC23-070 | 2.3 | 2.7 | 20.06 | $1.7^{+0.1}_{-0.2}$ | $3.5^{+0.1}_{-0.1}$ | $19.45^{+0.09}_{-0.30}$ | |
| A2199 | | | | | | | $-795^{+231}_{-553}$ |
| N 6158 | 11.4 | 12.8 | 21.75 | $11.2^{+0.1}_{-0.4}$ | $13.1^{+0.4}_{-0.1}$ | $21.71^{+0.02}_{-0.08}$ | |
| N 6166 | 57.2 | 14.1 | 23.54 | $57.1^{+0.1}_{-0.3}$ | $14.5^{+0.5}_{-0.2}$ | $23.54^{+0.00}_{-0.01}$ | |
| N6158COM | 4.2 | 4.8 | 21.75 | $3.7^{+0.1}_{-0.5}$ | $5.5^{+0.5}_{-0.2}$ | $21.50^{+0.07}_{-0.29}$ | |
| A2199Z34A | 10.6 | 10.2 | 21.95 | $10.4^{+0.1}_{-0.4}$ | $10.6^{+0.4}_{-0.1}$ | $21.90^{+0.02}_{-0.09}$ | |
| A2199-S18 | 5.1 | 8.7 | 21.15 | $4.7^{+0.1}_{-0.5}$ | $9.1^{+0.4}_{-0.1}$ | $20.97^{+0.05}_{-0.22}$ | |
| A2199-S24 | 8.6 | 2.8 | 23.26 | $8.3^{+0.1}_{-0.4}$ | $4.1^{+0.6}_{-0.3}$ | $23.19^{+0.03}_{-0.11}$ | |
| A2199-S26 | 10.2 | 7.9 | 22.22 | $10.0^{+0.1}_{-0.4}$ | $8.4^{+0.5}_{-0.2}$ | $22.17^{+0.02}_{-0.09}$ | |
| N6166FCOM | 4.0 | 4.9 | 21.66 | $3.5^{+0.1}_{-0.5}$ | $5.6^{+0.5}_{-0.2}$ | $21.38^{+0.08}_{-0.31}$ | |
| A2199-S30 | 3.1 | 8.5 | 20.45 | $2.5^{+0.1}_{-0.5}$ | $8.8^{+0.4}_{-0.1}$ | $20.00^{+0.11}_{-0.44}$ | |
| N6166NCOM | 2.9 | 3.6 | 21.63 | $2.3^{+0.1}_{-0.4}$ | $4.5^{+0.3}_{-0.2}$ | $21.12^{+0.12}_{-0.40}$ | |
| A2199-S33 | 3.8 | 7.4 | 20.93 | $3.3^{+0.1}_{-0.5}$ | $7.8^{+0.4}_{-0.1}$ | $20.63^{+0.08}_{-0.33}$ | |
| A2199-S34 | 3.4 | 5.6 | 21.19 | $2.9^{+0.1}_{-0.5}$ | $6.1^{+0.4}_{-0.2}$ | $20.81^{+0.10}_{-0.38}$ | |
| A2199-S44 | 3.4 | 7.2 | 20.85 | $2.9^{+0.1}_{-0.5}$ | $7.6^{+0.4}_{-0.1}$ | $20.47^{+0.10}_{-0.38}$ | |
| A2199-S43 | 4.4 | 6.9 | 21.30 | $4.0^{+0.1}_{-0.5}$ | $7.4^{+0.4}_{-0.2}$ | $21.07^{+0.07}_{-0.27}$ | |

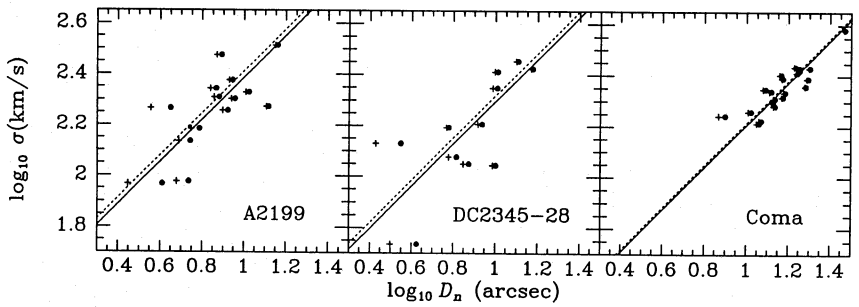


**Figure 11.** The $D_n$–$\sigma$ plots for the clusters A2199 (left), DC 2345 − 28 (middle), and Coma (right). Crosses show the data from Faber et al. (1989). Filled circles show the data when the seeing corrections described in Section 5 are applied (with FWHM = 2 arcsec). The full line shows the $D_n$–$\sigma$ relation derived using the corrected data, while the short-dashed line refers to the original data points.

derived from the average of the logarithms of the ratios $D_n^c/D_n$ for galaxies with $\sigma > 100$ km s$^{-1}$. This average corresponds to a spurious peculiar velocity of $-795$ km s$^{-1}$ ($\langle D_n^c/D_n \rangle = 0.93$) for A2199, and of $-577$ km s$^{-1}$ ($\langle D_n^c/D_n \rangle = 0.94$) for DC 2345 − 28. For comparison, the shift determined for 21 galaxies in the Coma cluster corresponds to $-159$ km s$^{-1}$ ($\langle D_n^c/D_n \rangle = 0.98$). For all three cluster the rms residual from the $D_n$–$\sigma$ relation is reduced when the seeing-corrected values of $D_n$ are adopted. The related error on the distance of the cluster is reduced from 11 to 9.5 per cent for A2199, from 17 to 15 per cent for DC 2345 − 28, and from 3.3 to 3.1 per cent for Coma, when seeing corrections are applied. The spurious peculiar velocity of A2199 is reduced to $-564$ km s$^{-1}$ if the $\Psi = 12$ model with the $\gamma = 1.8$ psf is considered, but can be as large as $-1348$ km s$^{-1}$ if the smoothed $R^{1/4}$ profile with the $\gamma = 1.4$ psf is used. Negative spurious peculiar velocities of the same order are derived when the fundamental plane equation of Faber et al. (1987) is used instead of the $D_n$–$\sigma$ relation. A discussion of the relative merits of the two approaches in estimating distances of ellipticals is beyond the scope of this paper (see Jørgensen et al. 1992).

Ironically, the effect of seeing on the observed peculiar velocity is less for clusters with only one or two apparently large galaxies observed, which is the case for most of the other distant Seven Samurai clusters. In the specific cases of A2162 and E115–G008 (Table 1), in which there is only one measured galaxy with large $R_e$, the seeing corrections amount to ~ 200 km s$^{-1}$.

We conclude that seeing effects can account for roughly 28 per cent of the measured peculiar velocity of A2199, and for all of the peculiar velocity of DC 2345 − 28. *Seeing effects must be taken into account when distant clusters at redshifts* $cz \gtrsim 8000$ km s$^{-1}$ *are studied.* However, since most of the Seven Samurai galaxies have large $R_e$, corrections for seeing are small and unlikely to affect the large-scale flow solutions of Lynden-Bell et al. (1988).

Lucey et al. (1991a) found that the cluster A2634 has a high peculiar velocity of −3400 km s$^{-1}$ when its distance is computed using the $D_n$–$\sigma$ relation. This value is at odds with the distance determined by Faber et al. (1989; see our Table 1) and with that determined using the Tully–Fisher relation for the spiral galaxies (Aaronson et al. 1986, 1989) in this cluster. Using the curves of Fig. 10, we estimate that only 150 km s$^{-1}$ could be still due to a residual seeing effect, if the smoothed model with the $\gamma = 1.5$ psf and FWHM = 1.5 arcsec is used to compute the corrections. Jørgensen et al. (1992) have shown that the large negative peculiar velocity of A2634 may be partially accounted for by the residual surface brightness dependence of the $D_n$–$\sigma$ relation for small galaxies.

## 6 CONCLUSIONS

We have presented a series of calculations and tests to study the effects of seeing on the photometric properties of elliptical galaxies, and in particular their use for estimating the distances of these galaxies. Our main results are as follows.

(1) A new family of functions for the analytical approximation of observed stellar profiles has been introduced, termed $p_\gamma$, which generalizes the predictions of atmospheric turbulence theory. A detailed comparison with observed star profiles shows that this new family gives significantly better fits than the widely used Moffat (1969) family.

(2) An extended survey of seeing convolutions with realistic model profiles of elliptical galaxies has been performed numerically. Three galaxy model profiles with different amounts of central concentration were tested: the $R^{1/4}$ law, the $\Psi = 12$ $f_\infty$ model, and an $R^{1/4}$ profile smoothed with a Gaussian. Note that all the models are azimuthally symmetric.

(3) The seeing-convolved profiles have been used to determine the ratios $R_e/R_e^c$ and $D_n/D_n^c$ and the corrections to surface brightnesses at and within $R_e$, $SB_e$ and $\langle SB_e \rangle$, as a function of $R_e^c$/FWHM and of $D_n^c/R_e^c$. These plots give a simple-to-use prescription to observers wishing to correct the raw values of the photometric parameters of elliptical galaxies. Half-luminosity radii derived from seeing-convolved profiles are larger than the true values, while $D_n$ diameters are smaller than the true ones. Mean effective surface brightnesses are fainter than the true ones. Seeing effects distort the $D_n$–$\sigma$ relation for small $D_n$, increasing the scatter relative to a power-law relation and producing a zero-point shift. A similar effect is observed when the fundamental plane equation is considered. Distances derived from data uncorrected for seeing are systematically larger than the true values, causing the radial peculiar velocities to be systematically too negative.

(4) We have applied the computed seeing corrections to the $D_n$–$\sigma$ data of the most distant clusters of the Seven Samurai sample (Faber et al. 1989), most of which have negative peculiar velocities. When seeing corrections are taken into account, the negative peculiar velocity of A2199 can be straightforwardly reduced by 28 per cent (795 km s$^{-1}$) and that of DC 2345 − 28 can be reduced from 565 km s$^{-1}$ to zero.

(5) Lucey et al. (1991a) have also considered the effects of seeing and have applied a correction to their $D_n$ measurements of the distant cluster A2634, for which they obtain (after correction) a large negative peculiar velocity. Our tests indicate that this correction should be sufficiently accurate to eliminate most of the seeing effect. The residual error is probably less than 150 km s$^{-1}$.

The results described here clearly show that seeing effects are important when one tries to measure the large-scale peculiar motions of galaxies at redshifts greater than 8000 km s$^{-1}$, as we are attempting to do in our EFAR survey. In order to minimize the effects of seeing, we plan to adopt the following approach in the analysis of the data. Since the effects of seeing on $D_n$ are smaller when the ratio $D_n/R_e$ is large (see Fig. 9), we shall determine our set of $D_n$ values at a fainter surface brightness than is normally chosen. When the canonical value of mean surface brightness is used (20.75 $B$ arcsec$^{-2}$), typically $D_n \approx R_e$. A decrease of 1 mag increases $D_n$ by about a factor of 4. The choice of a fainter surface brightness does not increase the scatter of the $D_n$–$\sigma$ relation (Lucey et al. 1991b).

## ACKNOWLEDGMENTS

RPS acknowledges the support of SFB 328, EB the support of NSF Grant AST90-01762, DB the support of NSF Grant AST90-16930, and RKM the support of NSF Grant AST90-20864. MC acknowledges the support of a Fellow-

ship at King's College, Cambridge. GW acknowledges partial support from NSF grant AST90-17048 and from Margaret Anne & Edward Leede '49. Support for travel and collaborative meetings was provided by NATO grant CRG900159, Dartmouth College and the University of Oxford. We all wish to thank the directors and staff of the MDM telescope and the JKT for their hospitality and unfailing aid during the observing runs.

## REFERENCES

Aaronson M., Bothun G., Mould J., Huchra J., Schommer R. A., Cornell M. E., 1986, ApJ, 302, 536
Aaronson M. et al., 1989, ApJ, 338, 654
Argyle R. W., Mayer C. J., Pike C. D., Jorden P. R., 1988, A User Guide to the JKT CCD Camera, La Palma User Manual No. XVIII. Royal Greenwich Observatory, Greenwich, p. A34
Bender R., Möllenhoff C., 1987, A&A, 177, 71
Bendinelli O., Lorenzutta S., Parmeggiani G., Zavatti F., 1984, A&A, 138, 337
Bendinelli O., Parmeggiani G., Zavatti F., 1987, JA&A, 8, 343
Bendinelli O., Parmeggiani G., Zavatti F., 1988, JA&A, 9, 17
Bendinelli O., Parmeggiani G., Zavatti F., Djorgovski S., 1990, AJ, 99, 774
Bertin G., Stiavelli M., 1984, A&A, 137, 26
Bertin G., Saglia R. P., Stiavelli M., 1988, ApJ, 330, 78
Bower R. G., Lucey J. R., Ellis R. S., 1992, MNRAS, 254, 589
Buonanno R., Buscema G., Lorsi C. E., Ferraro I., Iannicola G., 1983, A&A, 126, 278
Carter D., 1978, MNRAS, 182, 797
Cawson M. G. M., 1987, GRASP Documentation. University of Arizona, Tucson
Colless M., Burstein D., Wegner G., Saglia R. P., McMahan R., Davies R. L., Bertschinger E., Baggley G., 1993, MNRAS, 262, 475
Coulman C. E., 1985, ARA&A, 23, 19
De Lapparent V., Geller M. J., Huchra J. P., 1986, ApJ, 302, L1
de Vaucouleurs G., 1948, Ann. Astrophys., 11, 247
Djorgovski S., 1983, JA&A, 4, 271
Djorgovski S., Davis M., 1987, ApJ, 313, 42
Dressler A., Lynden-Bell D., Burstein D., Davies R. L., Faber S. M., Terlevich R. J., Wegner G., 1987, ApJ, 313, 42
Faber S. M., Dressler A., Davies R. L., Burstein D., Lynden-Bell D., Terlevich R. J., Wegner G., 1987, in Faber S. M., ed., Nearly Normal Galaxies From the Planck Time to the Present. Springer-Verlag, New York, p. 175
Faber S. M., Wegner G., Burstein D., Davies R. L., Dressler A., Lynden-Bell D., Terlevich R. J., 1989, ApJS, 63, 763
Franx M., Illingworth G., Heckman T., 1989, AJ, 98, 538
Fried D. L., 1966, J. Opt. Soc. Am., 56, 1372
Jørgensen I., Franx M., Kjærgaard P., 1992, in Danziger I. J., Zeilinger W. W., Kjär K., eds, Proc. ESO/EIPC Workshop, Structure, Dynamics and Chemical Evolution of Early-Type Galaxies, Isola d'Elba. ESO, Garching bei München, p. 71
King I. R., 1966, AJ, 71, 64
King I. R., 1971, PASP, 83, 199
Kormendy J., Richstone D., 1992, ApJ, 393, 559
Latham D., Da Costa L. N., eds, 1991, ASP Conf. Ser. 16, Large Scale Structures and Peculiar Motions in the Universe. Astron. Soc. Pac., San Francisco
Lauer T. R., 1985, ApJS, 57, 473
Lauer T. R. et al., 1992, AJ, 103, 703
Lucey R., Gray P. M., Carter D., Terlevich R. J., 1991a, MNRAS, 248, 804
Lucey R., Guzmán R., Carter D., Terlevich R. J., 1991b, MNRAS, 253, 584
Lynden-Bell D., Faber S. M., Burstein D., Davies R. L., Dressler A., Terlevich R. J., Wegner G., 1988, ApJ, 326, 19
Moffat A. F. J., 1969, A&A, 3, 455
Peletier R. F., Davies R. L., Illingworth G. D., Davis L. E., Cawson M., 1990, AJ, 100, 1091
Schweizer F., 1979, ApJ, 233, 23
Stiavelli M., Bertin G., 1985, MNRAS, 217, 735
Tody D., 1986, Proc. SPIE, 627, 733
Wegner G., Davies R. L., Colless M. M., Burstein D., Bertschinger E., McMahan R., 1991, in Latham D., Da Costa L. N., eds, ASP Conf. Ser. 16, Large Scale Structures and Peculiar Motions in the Universe. Astron. Soc. Pac., San Francisco, p. 129
Woolf N. J., 1982, ARA&A, 20, 367
Yee H. K. C., 1988, AJ, 95, 1331
Young P. J., Westphal J. A., Kristian J., Wilson C. P., Landauer F. P., 1978, ApJ, 221, 721

## APPENDIX A: NUMERICAL EVALUATION OF SEEING CONVOLUTIONS

In this appendix the numerical algorithms used to derive the results of Sections 2–4 are described. The relevant FORTRAN programs are available on request from R. P. Saglia (E-mail: G88@VM.URZ.UNI-HEIDELBERG.DE, SAGLIA@GAUSS.DM.UNIPI.IT).

Seeing is treated as a linear convolution of the true surface brightness distribution $I(\boldsymbol{R})$ with a psf $p(\boldsymbol{R})$ (equation 1). The convolutions are performed using Fourier transforms. The Fourier transforms pairs, illustrated for the psf, are

$$\hat{p}(\boldsymbol{k}) = \int \exp(\mathrm{i}\boldsymbol{k}\cdot\boldsymbol{R})\, p(\boldsymbol{R})\, \mathrm{d}^2R, \tag{A1}$$

$$p(\boldsymbol{R}) = \int \exp(-\mathrm{i}\boldsymbol{k}\cdot\boldsymbol{R})\, \hat{p}(\boldsymbol{k})\, \frac{\mathrm{d}^2k}{(2\pi)^2}. \tag{A2}$$

Notice that normalization implies $\hat{p}(0) = \hat{I}(0) = 1$. Using equations (1)–(2) and (A1)–(A2), the convolved surface brightness and the flux are

$$I^{\mathrm{c}}(\boldsymbol{R}) = \int \exp(\mathrm{i}\boldsymbol{k}\cdot\boldsymbol{R})\, \hat{p}(\boldsymbol{k})\, \hat{I}(\boldsymbol{k})\, \frac{\mathrm{d}^2k}{(2\pi)^2}, \tag{A3}$$

$$F^{\mathrm{c}}(R) = R \int J_1(kR)\, \hat{p}(\boldsymbol{k})\, \hat{I}(\boldsymbol{k})\, \frac{\mathrm{d}^2k}{2\pi k}. \tag{A4}$$

Equations (A3) and (A4) are exact. If we restrict ourselves to circular psf and profiles, $p = p(R)$, $I = I(R)$, then we obtain

$$I^{\mathrm{c}}(R) = \int_0^\infty J_0(kR)\, \hat{p}(k)\, \hat{I}(k)\, \frac{k\,\mathrm{d}k}{2\pi}, \tag{A5}$$

$$F^{\mathrm{c}}(R) = R \int_0^\infty J_1(kR)\, \hat{p}(k)\, \hat{I}(k)\, \mathrm{d}k. \tag{A6}$$

The Bessel functions $J$ arise from the relations

$$\int_0^{2\pi} \exp(\mathrm{i}kR\cos\theta)\, \mathrm{d}\theta = 2\pi J_0(kR), \tag{A7}$$

$$\int_0^x J_0(s)\, \mathrm{d}k = xJ_1(x). \tag{A8}$$

If the psf is circular but the profile is not, the angular integral in equation (A3) becomes simply an angular integral over the tranformed profile $\hat{I}(\boldsymbol{k})$. Equation (A6) gives the correct flux in circular apertures provided that $\hat{I}(\boldsymbol{k})$ is replaced by the angular average of $\hat{I}(\boldsymbol{k})$. Furthermore, the angular average may be performed first in the spatial domain (at fixed $R$), either before or after the convolution with seeing is performed, yielding exactly the same result. In short, for a circular psf one may circularly average the surface brightness distribution either before or after the convolution, and this may be done either in the spatial or spectral domain. The order of operations (circular averaging, convolution with psf) does not matter for a circular psf.

We assume a circular psf of the form given by equation (4). Because this psf is specified by its Fourier transform, equations (A5) and (A6) are ready to evaluate once we have the Fourier transform $\hat{I}(k)$ of the circularly averaged surface brightness distribution. The Fourier transforms of the $R^{1/4}$ and $f_\infty$ profiles were computed by numerical integration of equation (A1) (substituting $I$ for $p$). The smoothed $R^{1/4}$ profile was obtained by multiplying $\hat{I}(k)$ for the $R^{1/4}$ law by $\exp(-k^2R_s^2/2)$, where $R_s=0.017R_e$ is the smoothing radius. The numerical integration of $\hat{I}(k)$ was made delicate by the sharp cores of these profiles, but results with a relative accuracy of about $1\times10^{-4}$ were obtained. The results for the $R^{1/4}$ law may be summarized by the following analytical fit:

$$\hat{I}(k)=\left(\frac{1+a_1k+a_2k^2+a_3k^3+a_4k^4+a_5k^5}{1+a_1k+a_6k^2+a_7k^3+a_8k^4+a_9k^5+a_{10}k^6}\right)^{3/2}, \quad \text{(A9)}$$

where $a_1=7.3264$, $a_2=3.7241$, $a_3=-1.8154\times10^{-2}$, $a_4=1.7078\times10^{-3}$, $a_5=2.5032\times10^{-5}$, $a_6=8.1872$, $a_7=1.5431$, $a_8=-6.4540\times10^{-3}$, $a_9=7.8400\times10^{-4}$ and $a_{10}=1.1589\times10^{-5}$, and $k$ has units of $R_e^{-1}$. This fit has a relative accuracy of $1\times10^{-3}$ or better for all $k$. The transform of the $\Psi=12\,f_\infty$ model is not as easy to fit. Accurate interpolation tables of the Fourier transforms for both models are available on request (see e-mail address given above).

The elliptical model profiles have a one-dimensional length-scale parameter, $R_e$. Similarly, the psfs have one length-scale, FWHM. The convolution of the two profiles therefore gives a two-parameter family of surface brightness and flux: $I^c=I^c(2R/\mathrm{FWHM},\ \mathrm{FWHM}/2R_e)$, $F^c=F^c(2R/\mathrm{FWHM},\ \mathrm{FWHM}/2R_e)$. Our tables are recorded in this two-dimensional form. More than two dimensions would be required if the profile or psf were non-circular. A comparison of the values of $F^c$ for the $R^{1/4}$ model and the $p_\gamma$ function with $\gamma=5/3$ with those derived by Bower et al. (1992) is given in Fig. 7 and shows that the differences are less than 0.01 mag.